Broadband Anisotropic Photoresponse of the "Hydrogen Atom" Version Type-II Weyl Semimetal Candidate TaIrTe₄

Jiawei Lai,[†] Yinan Liu,[†] Junchao Ma,[†] Xiao Zhuo,[†] Yu Peng,[‡] Wei Lu,[†] Zheng Liu,[‡,||] Jianhao Chen,*,[†,§] and Dong Sun*,[†,§]

[†]International Center for Quantum Materials, School of Physics, Peking University, Beijing 100871, P. R. China

[‡]Centre for Programmed Materials, School of Materials Science and Engineering, Nanyang Technological University, Singapore 639798, Singapore

[§]Collaborative Innovation Center of Quantum Matter, Beijing 100871, P. R. China

[||]NOVITAS, Nanoelectronics Centre of Excellence, School of Electrical and Electronic Engineering, Nanyang Technological University, Singapore 639798, Singapore

ABSTRACT: The layered ternary compound TaIrTe₄ is an important candidate to host the recently predicted type-II Weyl Fermions that break Lorentz invariance. Photodetectors based on Weyl semimetal promise extreme performance in terms of highly sensitive, broadband, and self-powered operation owing to its topologically protected band structures. In this work, we report the realization of a broadband self-powered photodetector based on TaIrTe₄. The photocurrent generation mechanisms are investigated with power- and temperature-dependent photoresponse measurements. The prototype metal-TaIrTe₄-metal photodetector exhibits a responsivity of 20 μA W^{-1} or a specific detectivity of 1.8×10^6 Jones with 27 μs response time at 10.6 μm. Broadband responses from 532 nm to 10.6 μm are experimentally tested with potential detection range extendable to far-infrared and terahertz. Furthermore, anisotropic response of the TaIrTe₄ photodetector is identified using polarization-angle-dependent measurement with linearly polarized light. The anisotropy is found to be wavelength dependent, and the degree of anisotropy increases as the excitation wavelength gets closer to the Weyl nodes. Our results suggest this emerging class of materials can be harnessed for broadband, polarization angle-sensitive, self-powered photodetection with reasonable responsivities.

KEYWORDS: Weyl semimetal, photodetector, anisotropic response, mid-infrared, thermoelectric, 2D layered materials
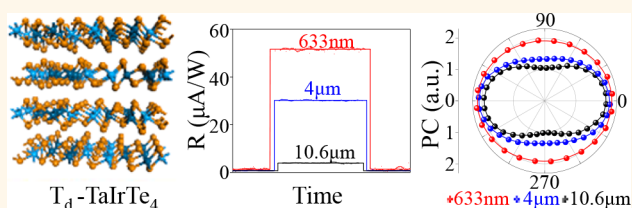
R oom-temperature operated, self-powered, integratable, and portable photosensing devices are highly appealing and of practical importance owing to their wide range of applications in imaging, remote sensing, environmental monitoring, optical communications, and analytical applications.[1−3] While such photodetectors are commercially available and quite matured in the visible and near-IR wavelength region, mainly based on conventional semiconductor materials such as silicon and InGaAs, the applications of photodetectors in the mid-IR wavelength region, based on narrow bandgap semiconductors HgCdTe[4] and InSb,[5,6] are quite limited by the requirement of cryogenic temperature operation. Room-temperature operation of mid-IR photodetector with high detectivity remains a technical challenge so far,[7,8] though many novel materials and structures are explored for this purpose recently.[3,9−11] As it is more easily to form good contact with typical contact metal electrodes, semimetal is more favorable than gapped semiconductor for self-powered operation, which can avoid the dark current without light illumination under a voltage bias. On the other hand, Dirac semimetals (DSMs), which have time reversal and space inversion symmetry such as graphene and Cd₃As₂, were found to exhibit broadband detection from ultraviolet (UV) to terahertz (THz) range, lower dark current, ultrafast response time, and tunable optical properties *via* electrostatic doping.[12−16]

Weyl semimetals (WSMs) is a topological semimetal with broken time reversal or inversion symmetry, in which energy bands also disperse linearly in three-dimensional momentum space.[17,18] Depending on the violation of Lorentz invariance, WSMs are classified into two types: Type-I WSM has Weyl points (WPs) associated with a closed point-like Fermi surface,[19−24] while the WPs of Type-II appears at the boundary of electron and hole pockets.[25] Due to these differences, the type-II WSM exhibits very different transport properties from
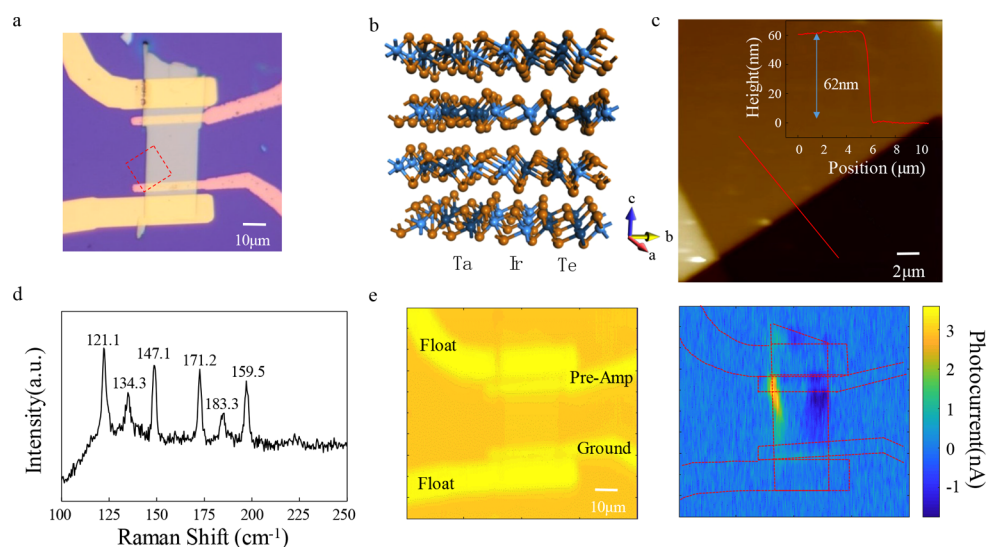
Figure 1. Basic characterization of the TaIrTe$_4$ sample. (a) Optical image of a TaIrTe$_4$ device. (b) Crystal structures of TaIrTe$_4$ in the T_d phase. (c) AFM image of the TaIrTe$_4$ device. The scanning range is shown in (a) as a red box. Inset indicates thickness of the sample. The height section profile is shown as the red line in (c). (d) Characteristic Raman spectra of TaIrTe$_4$. (e) SPCM images of the TaIrTe$_4$ device at room temperature with 800 nm excitation. Left and right panels show the reflection image and PC image, respectively.
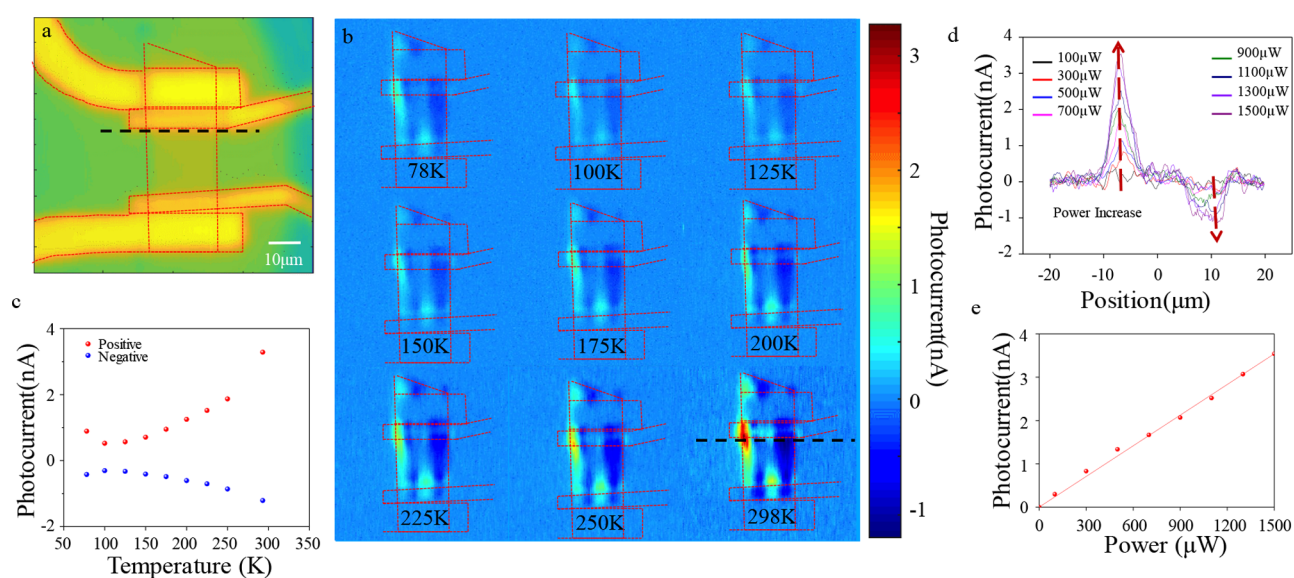
Figure 2. Excitation power- and temperature-dependent PC measurement of TaIrTe$_4$. (a) SPCM reflection image of the TaIrTe$_4$ device. The red dash lines indicate the outline of the electrodes and the sample. (b) SPCM images of the TaIrTe$_4$ device at temperatures 78, 100, 125, 150, 175, 200, 225, 250, and 298 K with 800 nm excitation wavelength and 500 μW excitation power. (c) The maximum positive (red) and negative (blue) PC response under different temperatures. (d) Photocurrent response of the TaIrTe$_4$ device along the 40 μm line cut, marked as black line in (a) and (b), under different excitation powers varying from 100 to 1500 μW at 298 K. (e) The positive PC response as a function of excitation power. The solid lines represent the linear fit.

Type-I WSM.[25,26] When used as photodetectors, WSMs share many advantages with the well-studied DSMs including broadband photothermoelectric (PTE) effect response due to the gapless semimetallic band structure and high responsivity as a result of linear dispersion and suppressed back scattering.[27−30] In addition, the responsivity is greatly enhanced by the extremely high carrier mobility around the Weyl node, comparable or even exceeding that of graphene.[31] On the other hand, similar to Cd$_3$As$_2$, the linear dispersion holds along all the three dimensions over a certain energy range, which ensures the efficient carrier transport along all the directions.[32] Furthermore, WSMs have distinct advantage over DSMs that is related

to the chiral Fermions near the Weyl node, which leads to chirality-dependent photocurrent (PC).[33]

In this work, we investigate the performance of a field effect photodetector device based on the type-II WSM candidate, layered ternary compound TaIrTe$_4$. TaIrTe$_4$ is an important candidate to host the theoretically predicted type-II Weyl Fermions, recent Raman characterization has provided definite proof of the absence of inversion symmetry, a prerequisite for the existence of Weyl Fermions. Compared to the experimentally verified type-I WSM TaAs family with 24 WPs and type-II WSM MoTe$_2$ family[34−36] with 8 WPs, TaIrTe$_4$ hosts only four WPs, the minimal number of WPs a WSM with time-reversal invariance can host.[26,35,37−39] Thus, TaIrTe$_4$ offers the
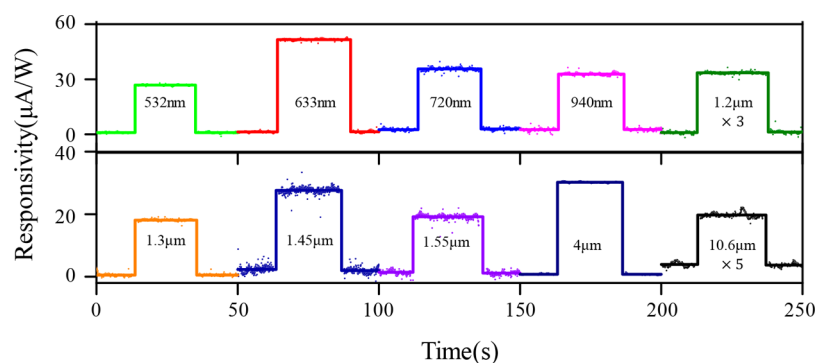
Figure 3. Broadband photoresponse of TaIrTe$_4$ photodetector. Photoresponse of the TaIrTe$_4$ device for different excitation wavelengths at 298 K. For better visualization, the magnitude of low responsivities obtained for different wavelengths is multiplied.

simplest "hydrogen atom" example of an inversion-breaking Weyl semimetal.[37] In addition, TaIrTe$_4$ also hosts larger Fermi arc surface states compared to the MoTe$_2$ family, allowing sample momentum space for experimental studies of topological related properties. For these reasons, TaIrTe$_4$ is a practically important model type-II WSM and an ideal material platform for device applications. Considering the essence of WSMs, in this work, a field effect TaIrTe$_4$-based photodetector has been studied over a broadband wavelength regime (from visible 532 nm to the mid-infrared 10.6 μm) working in unbiased self-powered mode at room temperature. The responsivities and specific detectivities can reach 0.34 mA W^{-1} and 2.7 × 10^7 Jones at 633 nm, 30.2 μA W^{-1} and 2.5 × 10^6 Jones at 4 μm, and 20 μA W^{-1} and 1.4 × 10^6 Jones at 10.6 μm, respectively. It also exhibits fast response time in the range of 25−30 μs over broad wavelength range. Moreover, the polarization-dependent study revealed a highly anisotropic photoresponse of TaIrTe$_4$. Although 2D layered black phosphorus (BP)[40,41] has shown similar anisotropic response, the application of BP for this purpose is limited by the 0.3 eV bandgap. Considering the ambient stability of TaIrTe$_4$ is much better than BP, TaIrTe$_4$ provides a complementary solution for BP over a long wavelength beyond 4 μm in terms of polarization angle-sensitive photodetection.

RESULTS AND DISCUSSION

The photoresponse measurements are performed on the mechanically exfoliated flakes of TaIrTe$_4$, obtained from the bulk TaIrTe$_4$, synthesized by chemical vapor deposition (CVD) method. The exfoliated TaIrTe$_4$ flakes are fabricated into lateral metal-TaIrTe$_4$-metal devices as shown in Figure 1a. The inner two electrodes are connected for PC measurement. Figure 1b shows the crystal structure of TaIrTe$_4$ that has T_d phase which belongs to noncentrosymmetric space group ($Pmn2_1$). The characteristic Raman spectra of the exfoliated 62 nm-thick TaIrTe$_4$ (AFM image shown in Figure 1c) are shown in Figure 1d. Figure 1e illustrates a typical scanning PC measurement (SPCM) image of a TaIrTe$_4$ device together with its *in situ* scanning reflection microscopy with 800 nm excitation and about 3 μm spatial resolution. The dimension of the sample between the two inner electrodes is about 20 μm × 40 μm, and the PC response can be obtained from the whole device, which includes both the interface of TaIrTe$_4$-metal junctions and the inner area of TaIrTe$_4$ that are away from the metal electrodes. In addition, we note although the stability of few layer TaIrTe$_4$ is poor in the air, the photoresponse and transport properties of the TaIrTe$_4$ devices turn out to be very stable under ambient

conditions over several months. This is because the major layers underneath the surface are well protected from degradation for devices made from relatively thick flakes.

Figure 2 illustrates the temperature- and excitation power-dependent measurements at 800 nm with reflection image shown in Figure 2a. The temperature dependence is measured from room temperature down to 78 K. The SPCM patterns recorded at different temperatures (illustrated in Figure 2b) remain qualitatively the same. The positive/negative maximum PC response amplitudes at different temperatures are shown in Figure 2c. The magnitude of PC response decreases slightly as temperature varies from 78 to 100 K and then increases monotonically with temperature up to 298 K. The effect of excitation power on the PC response is measured by scanning through a line cut crossing the maximum and minimum PC response of the device, as marked by the black line cuts in Figure 2a,b. The power-dependent measurements are carried out at 298 K by varying the power from 100 to 1500 μW. The shape and peak position of photoresponse along the line cut remains unaffected at different excitation power (Figure 2d). Furthermore, the magnitude of PC response increases linearly with power, as shown in Figure 2e. The nonlocal PC generation away from the contact region and the temperature dependence of the PC amplitude implies the photothermoelectric effect (PTE) plays a crucial role in the PC generation.The PC generation from PTE effect does not rely on the proximity of contacts and thus can contribute to the "nonlocal" response away from the two electrodes through the well-known Shockley−Ramo mechanism similar to graphene.[42] However, either photovoltaic (PV) effect or photo-Dember (PD) effect relies on the metal electrode, thus the PC generated from PV and PD is highly localized and can only happen at the metal-TaIrTe$_4$ interface.[10,32] The nonmonotonic temperature dependence of PC amplitude further confirms that the PTE effect contributes to the photoresponse. The magnitude of the PC from the PTE effect can have complicated lattice temperature dependence as shown in Figure 2c, because both the Seebeck coefficient and heat capacitance depend on temperature. For PV and PD, the response should decrease as temperature increases, as the mobility is found to decrease monotonically with increasing temperature through transport measurement, while built-in electric field is not sensitive to the temperature.

Taking the advantage of gapless linear dispersion band structure, the PC responses of the TaIrTe$_4$ device should spread over a broad wavelength range. Figure 3 illustrates the short-circuit PC responses at different excitation photon energies ranging from 0.12 to 2.33 eV on the TaIrTe$_4$ device.

Table 1. Comparison of Broadband Photodetectors

material	responsivity	response time	spectral range (μm)	ref	notes
graphene	6.1 mA/W	62.5 ps	UV–SWIR	44	broadband
Cd$_3$As$_2$	5.9 mA/W	6.9 ps	0.532–10.6	32	broadband
InSb	0.1 A/W	0.1 ns	2.5–8	5, 6	300 K
HgCdTe	0.3 A/W	2.2 ns	3–10	45	300 K
	0.6 A/W	100 ns	2–14	46	77 K
TaIrTe$_4$	0.02 mA/W	27 μs	0.532–10.6	this work	broadband
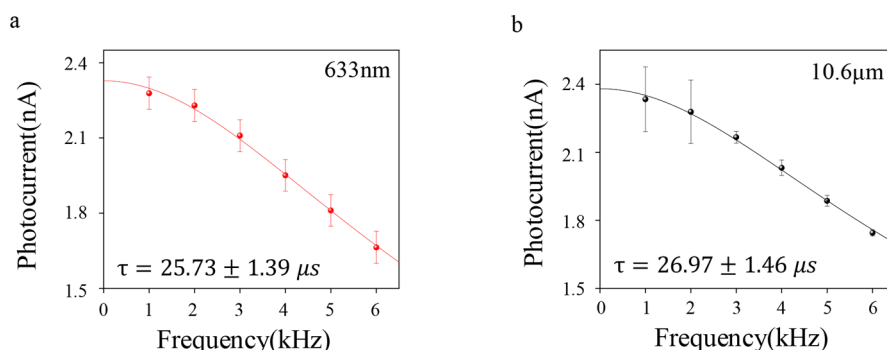
Figure 4. Response time of TaIrTe$_4$ photodetector. (a,b) Chopping frequency-dependent responsivity measurement with a lock-in amplifier under 633 nm and 10.6 μm excitation, respectively. The deducted response time of different wavelengths are labeled in the figure.
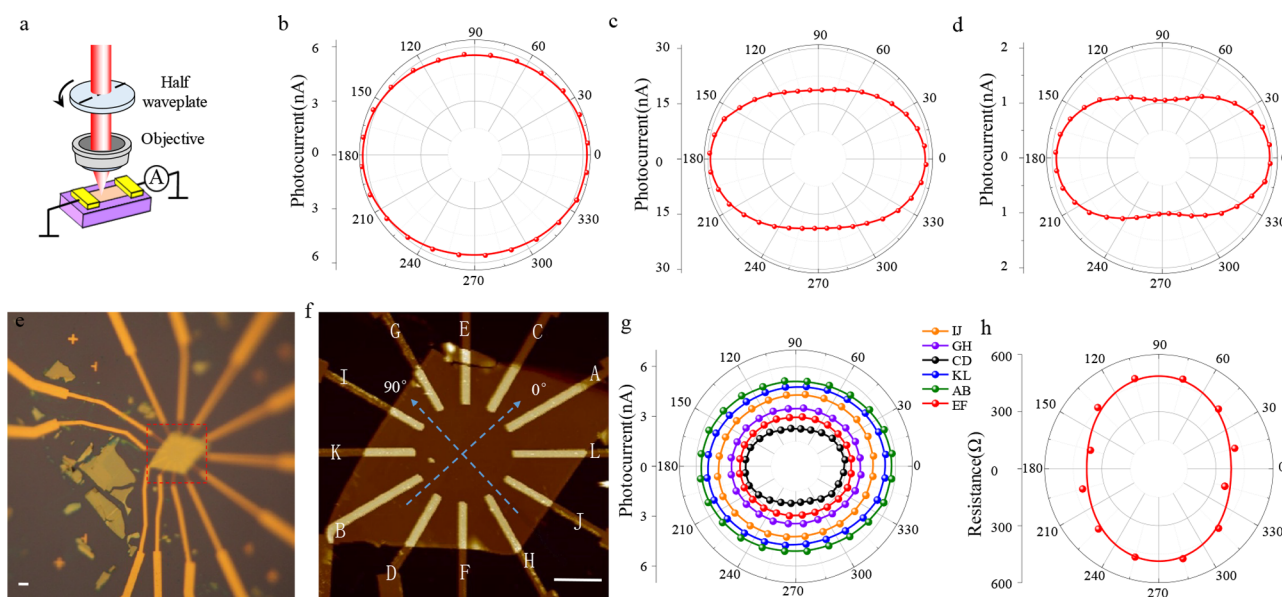
Figure 5. Anisotropy photoresponse of TaIrTe$_4$ photodetector. (a) Schematic representation of linear polarization-dependent PC measurement setup. (b–d) Anisotropic PC response for the linear polarized excitation at 633 nm, 4 μm, and 10.6 μm, respectively. The ratios of anisotropy ellipse are 1.13, 1.56, and 1.88, respectively. (e) Optical image of the device with 12 electrodes. (f) AFM image of the device with 12 electrodes. (g) Anisotropic PC response for each pair of diagonal electrodes. The electrodes are labeled in (f). (h) Anisotropic resistance for each pair of diagonal electrodes. The orientation of zero degree is shown in (f). All scale bars indicate 5 μm.

In wavelength-dependent measurement, the PC responses at 0.12 and 0.31 eV are recorded using two continuous wave (CW) quantum cascade laser sources, while the responses from 0.80 to 2.33 eV are recorded by switching on/off the laser pulse (6 ps, 20 MHz) from a fiber-based white light supercontinuum source. Since the PC is measured with very different light sources at different wavelengths, it is to be noted that a direct comparison of specific detectivities for different wavelengths is quite difficult because of different focused laser spot sizes and instantaneous excitation energies. The PC responses for different excitation photon energies are measured at the maximum of positive PC as marked by the red circle in the SPCM shown in Figure 3c at zero bias voltage. The responsivity and detectivity for the lowest excitation energy (0.12 eV) are found to be 20 μA W^{-1} and 1.4 × 10^6 Jones, whereas the highest responsivity and detectivity are 0.34 mA W^{-1} and 2.7 × 10^7 Jones, respectively, occurring at excitation energy of 1.96 eV. A brief comparison of the device performance between Dirac Semimetals (graphene and Cd$_3$As$_2$) and commercial mid-infrared photodetector (HgCdTe and InSb) is shown in Table 1. We note epitaxial growth techniques can potentially be developed for these listed

materials, to make them compatible with standard CMOS technology. It is worth noting that the response wavelength range is limited by the availability of light sources rather than by the response of the device itself. As a gapless WSM, TaIrTe$_4$ should possess an ultrabroadband response extendable to much lower photon energy even down to THz, similar to graphene and Cd$_3$As$_2$.[43] The response of the device is relatively low as a result of inefficient extraction of photocarriers due to the metallic nature of the material. However, we note the responsivity at longer wavelength beyond 10.6 μm could be much higher when the optical transition gets closer to the Weyl nodes, where the carrier mobility is much higher due to the linear energy dispersion and suppression of backscattering. The overall responsivity can be further enhanced using different source drain metals with interdigitated contacts to provide opposite built-in electric field directions with TaIrTe$_4$, thus avoiding the cancellation of the PC when illuminated with light spot larger than the active device channel area.[44] The PC response due to the PTE mechanism could be further enhanced by fabricating suspended device over the substrate to reduce cooling through the substrate. Figure 4 shows the response time measurement through standard chopping frequency-dependent responsivity measurement at different wavelengths. The response times are 25.73 and 26.97 μs at 633 nm and 10.6 μm, respectively.

At last, the linear polarization-dependent PC responses of TaIrTe$_4$ are studied by varying the polarization of the excitation beam at different wavelengths as illustrated in Figure 5a. The polar plot of PC response at a fixed position of the device with different excitation polarization angles at 633 nm, 4 μm, and 10.6 μm are shown in Figure 5b–d, respectively. Interestingly, the device shows anisotropic response to the angle of linearly polarized light, similar to BP,[9,47,48] with the only difference that the response is anisotropic at all wavelengths. The anisotropy ratio, which is defined as the ratio between long and short axes of the ellipse, is 1.13, 1.56, and 1.88 for 633 nm, 4 μm, and 10.6 μm, respectively. The wavelength dependence of the anisotropy ratio indicates the response is more anisotropic when excited with lower photon energy. A likely explanation of the anisotropy is the different effective masses and thus different absorption along the two axes of the TaIrTe$_4$ crystals.[49−52] Similar anisotropic response is also observed on other Type-II Weyl semimetal candidates.[49] Furthermore, to investigate if the anisotropic response is a pure material property of TaIrTe$_4$ or if it is the result of a specific device structure,[53,54] a device with 12 electrodes uniformly distributed on the sample was fabricated, as shown in Figure 5e. Linear polarization dependence of PC was measured between each pair of diagonal contacts with an excitation wavelength of 633 nm and excitation power of 200 μW. The results (shown in Figure 5g) indicate that the orientations of the ellipses are the same, which means the anisotropic response is independent of electrode configuration and it is solely decided by the crystal orientation of TaIrTe$_4$. Thus, the a- and b-axes of the TaIrTe$_4$ could be independently determined using the polarization-angle-resolved PC response measurement, with the maximum PC response along the high mobility a-axis. In addition, the resistance between each pair of electrodes along different crystal directions is different, as shown in Figure 5h, where the low resistance direction is consistent with the high mobility direction along the crystal a-axis. The polarization angle-sensitive photoresponse of TaIrTe$_4$ is very similar to that of BP, which is suitable for polarization-sensitive photodetection. However, in contrast to BP, where the

sensing wavelength range of BP is limited by the 4 μm bandgap, the detectable wavelength of TaIrTe$_4$ photodetectors can be extended beyond 4 μm, and is more anisotropic at longer wavelength.

CONCLUSIONS

In summary, the physical properties of Type-II WSM TaIrTe$_4$ enable self-powered broadband photodetectors operating at room temperature with polarization angle-sensitive response. The self-powered operation could greatly facilitate wearable and portable applications, in particular wearable mid-IR sensing applications. As a 2D layered material, TaIrTe$_4$ could further incorporate many other possibilities by convenient integration with other layered 2D materials through van der Waals heterostructures.[55−57] In this regard, the layered TaIrTe$_4$ is endowed with great potential, surpassing the 3D Dirac semimetal Cd$_3$As$_2$ which processes similar advantages in terms of responsivity and broadband response as a photo-sensing material.

MATERIALS AND METHODS

Sample Growth. All the elements used in sample growth were stored and acquired in an argon-filled glovebox with moisture and oxygen levels <0.1 ppm, and all manipulations were carried out in the glovebox. TaIrTe$_4$ single crystals were synthesized by solid-state reaction with the help of Te flux. The elements of Ta powder (99.99%), Ir powder (99.999%), and Te lump (99.999%) with an atomic ratio of Ta/Ir/Te = 1:1:12, purchased from Sigma-Aldrich (Singapore), were loaded in a quartz tube and then flame-sealed under high-vacuum of 10^{-6} Torr. The quartz tube was placed in a tube furnace, slowly heated up to 1000 °C and held for 100 h, and then allowed to cool to 600 °C at a rate of 0.8 °C/h, followed by a cool down to room temperature.

Device Fabrication. The thin TaIrTe$_4$ samples used for the studies in this work were mechanically exfoliated from bulk TaIrTe$_4$ crystal and transferred on to 300 nm SiO$_2$/Si substrates. The thickness of TaIrTe$_4$, measured by atomic force microscopy (AFM), was estimated to be 62 nm (shown in Figure 1c). Standard electron-beam lithography technique was used to pattern electrodes, two-terminals, consisting of 5 nm Cr and 50 nm Au.

Raman Characterization. The Raman spectra were carried out on a HR 800 (Jobin Yvon Horiba), with a 632.8 nm laser. Raman measurements were carried out in ambient conditions, since the TaIrTe$_4$ flakes were fairly air stable.

Photoresponse Measurements. Standard scanning PC measurements were performed in ambient conditions using 800 nm CW laser with ~2 μm spatial resolution. The laser beam was focused by a 40× transmissive objective lens, and a scanning mirror was used to scan the light beam on the sample. The laser beam was modulated with a mechanical chopper (383 Hz), and the short-circuit PC signal was detected with a current preamplifier and a lock-in amplifier. The reflection signal and PC were recorded simultaneously to get the reflection image and PC response. For wavelength-dependent measurements, a series of bandpass filters were used to select the desired wavelength from a white light supercontinuum output of Fianium: WhiteLase-Micro (20 MHz, 6 ps, 450−2200 nm). Two CW quantum cascade laser sources emitting at 4 and 10.6 μm were used for mid-infrared measurement. The mid-IR beams were focused by a 40× reflection objective with a spot diameter of about 8 μm and 18 μm for 4 μm and 10.6 μm excitation, respectively. However, for polarization-dependent PC measurements, the 632.8 nm, 4 μm, and 10.6 μm laser beams are all focused to spot diameters of about 20 μm instead. The large focus spot helped to avoid the possible effect of sample drift during the measurements. A motorized rotation stage was used to rotate a half waveplate for the linear polarization-dependent measurement. Response time measurements were performed in ambient conditions using CW excitation and an optical chopper

with different chopping frequencies. The PC response (R_f) taking from a lock-in amplifier as a function of the different chopping frequencies (f) were fitted with $R_f = R_0/\sqrt{1 + (2\pi f\tau)^2}$ to obtain the response time (τ).

AUTHOR INFORMATION

Corresponding Authors
*E-mail: sundong@pku.edu.cn.
*E-mail: chenjianhao@pku.edu.cn.

ORCID
Zheng Liu: 0000-0002-8825-7198
Dong Sun: 0000-0002-0898-4548

Author Contributions
D.S. conceived the idea and designed the experiments; J.C.M. and X.Z. performed the optical measurements under the supervision of D.S.; Y.P. and Z.L. provided the bulk TaIrTe$_4$ materials; Y.N.L. fabricated the TaIrTe$_4$ devices and performed the sample characterization under the supervision of J.H.C.; J.W.L., J.C.M., J.H.C., and D.S. analyzed the results; J.W.L. wrote the manuscript, assisted by D.S. Y.N.L., J.C.M., X.Z., W.L., and J.H.C; and all the authors commented on the manuscript.

Notes
The authors declare no competing financial interest.

REFERENCES
(1) Koppens, F. H.; Mueller, T.; Avouris, P.; Ferrari, A. C.; Vitiello, M. S.; Polini, M. Photodetectors Based on Graphene, Other Two-Dimensional Materials and Hybrid Systems. *Nat. Nanotechnol.* **2014**, *9*, 780−793.
(2) Zhang, B. Y.; Liu, T.; Meng, B.; Li, X.; Liang, G.; Hu, X.; Wang, Q. J. Broadband High Photoresponse from Pure Monolayer Graphene Photodetector. *Nat. Commun.* **2013**, *4*, 1811.
(3) Liu, C. H.; Chang, Y. C.; Norris, T. B.; Zhong, Z. Graphene Photodetectors with Ultra-Broadband and High Responsivity at Room Temperature. *Nat. Nanotechnol.* **2014**, *9*, 273−278.
(4) Rogalski, A. HgCdTe Infrared Detector Material: History, Status and Outlook. *Rep. Prog. Phys.* **2005**, *68*, 2267−2336.
(5) Kimukin, I.; Biyikli, N.; Kartaloglu, T.; Aytur, O.; Ozbay, E. High-Speed InSb Photodetectors on GaAs for Mid-IR Applications. *IEEE J. Sel. Top. Quantum Electron.* **2004**, *10*, 766−770.
(6) Michel, E.; Xu, J.; Kim, J. D.; Ferguson, I.; Razeghi, M. InSb Infrared Photodetectors on Si Substrates Grown by Molecular Beam Epitaxy. *IEEE Photonics Technol. Lett.* **1996**, *8*, 673−675.
(7) Rogalski, A. Infrared Detectors: Status and Trends. *Prog. Quantum Electron.* **2003**, *27*, 59−210.
(8) Wang, Q. S.; Lai, J. W.; Sun, D. Review of Photo Response in Semiconductor Transition Metal Dichalcogenides Based Photosensitive Devices. *Opt. Mater. Express* **2016**, *6*, 2313−2327.
(9) Buscema, M.; Groenendijk, D. J.; Blanter, S. I.; Steele, G. A.; van der Zant, H. S.; Castellanos-Gomez, A. Fast and Broadband Photoresponse of Few-Layer Black Phosphorus Field-Effect Transistors. *Nano Lett.* **2014**, *14*, 3347−3352.

(10) Buscema, M.; Island, J. O.; Groenendijk, D. J.; Blanter, S. I.; Steele, G. A.; van der Zant, H. S.; Castellanos-Gomez, A. Photocurrent Generation with Two-Dimensional Van Der Waals Semiconductors. *Chem. Soc. Rev.* **2015**, *44*, 3691−3718.
(11) Wang, P.; Liu, S.; Luo, W.; Fang, H.; Gong, F.; Guo, N.; Chen, Z. G.; Zou, J.; Huang, Y.; Zhou, X.; Wang, J.; Chen, X.; Lu, W.; Xiu, F.; Hu, W. Arrayed Van Der Waals Broadband Detectors for Dual-Band Detection. *Adv. Mater.* **2017**, *29*, 1604439.
(12) Xia, F.; Mueller, T.; Lin, Y. M.; Valdes-Garcia, A.; Avouris, P. Ultrafast Graphene Photodetector. *Nat. Nanotechnol.* **2009**, *4*, 839−843.
(13) Sun, D.; Aivazian, G.; Jones, A. M.; Ross, J. S.; Yao, W.; Cobden, D.; Xu, X. Ultrafast Hot-Carrier-Dominated Photocurrent in Graphene. *Nat. Nanotechnol.* **2012**, *7*, 114−118.
(14) Tielrooij, K. J.; Piatkowski, L.; Massicotte, M.; Woessner, A.; Ma, Q.; Lee, Y.; Myhro, K. S.; Lau, C. N.; Jarillo-Herrero, P.; van Hulst, N. F.; Koppens, F. H. Generation of Photovoltage in Graphene on a Femtosecond Timescale through Efficient Carrier Heating. *Nat. Nanotechnol.* **2015**, *10*, 437−443.
(15) Li, Z. Q.; Henriksen, E. A.; Jiang, Z.; Hao, Z.; Martin, M. C.; Kim, P.; Stormer, H. L.; Basov, D. N. Dirac Charge Dynamics in Graphene by Infrared Spectroscopy. *Nat. Phys.* **2008**, *4*, 532−535.
(16) Wang, F.; Zhang, Y.; Tian, C.; Girit, C.; Zettl, A.; Crommie, M.; Shen, Y. R. Gate-Variable Optical Transitions in Graphene. *Science* **2008**, *320*, 206−209.
(17) Wan, X. G.; Turner, A. M.; Vishwanath, A.; Savrasov, S. Y. Topological Semimetal and Fermi-Arc Surface States in the Electronic Structure of Pyrochlore Iridates. *Phys. Rev. B: Condens. Matter Mater. Phys.* **2011**, *83*, 205101.
(18) Weng, H. M.; Fang, C.; Fang, Z.; Bernevig, B. A.; Dai, X. Weyl Semimetal Phase in Noncentrosymmetric Transition-Metal Monophosphides. *Phys. Rev. X* **2015**, *5*, 011029.
(19) Huang, S. M.; Xu, S. Y.; Belopolski, I.; Lee, C. C.; Chang, G.; Wang, B.; Alidoust, N.; Bian, G.; Neupane, M.; Zhang, C.; Jia, S.; Bansil, A.; Lin, H.; Hasan, M. Z. A Weyl Fermion Semimetal with Surface Fermi Arcs in the Transition Metal Monopnictide TaAs Class. *Nat. Commun.* **2015**, *6*, 7373.
(20) Lv, B. Q.; Xu, N.; Weng, H. M.; Ma, J. Z.; Richard, P.; Huang, X. C.; Zhao, L. X.; Chen, G. F.; Matt, C. E.; Bisti, F.; Strocov, V. N.; Mesot, J.; Fang, Z.; Dai, X.; Qian, T.; Shi, M.; Ding, H. Observation of Weyl Nodes in TaAs. *Nat. Phys.* **2015**, *11*, 724−727.
(21) Yang, L. X.; Liu, Z. K.; Sun, Y.; Peng, H.; Yang, H. F.; Zhang, T.; Zhou, B.; Zhang, Y.; Guo, Y. F.; Rahn, M.; Prabhakaran, D.; Hussain, Z.; Mo, S. K.; Felser, C.; Yan, B.; Chen, Y. L. Weyl Semimetal Phase in the Non-Centrosymmetric Compound TaAs. *Nat. Phys.* **2015**, *11*, 728−732.
(22) Lv, B. Q.; Weng, H. M.; Fu, B. B.; Wang, X. P.; Miao, H.; Ma, J.; Richard, P.; Huang, X. C.; Zhao, L. X.; Chen, G. F.; Fang, Z.; Dai, X.; Qian, T.; Ding, H. Experimental Discovery of Weyl Semimetal TaAs. *Phys. Rev. X* **2015**, *5*, 031013.
(23) Huang, X. C.; Zhao, L. X.; Long, Y. J.; Wang, P. P.; Chen, D.; Yang, Z. H.; Liang, H.; Xue, M. Q.; Weng, H. M.; Fang, Z.; Dai, X.; Chen, G. F. Observation of the Chiral-Anomaly-Induced Negative Magnetoresistance in 3D Weyl Semimetal TaAs. *Phys. Rev. X* **2015**, *5*, 031023.
(24) Xu, B.; Dai, Y. M.; Zhao, L. X.; Wang, K.; Yang, R.; Zhang, W.; Liu, J. Y.; Xiao, H.; Chen, G. F.; Taylor, A. J.; Yarotski, D. A.; Prasankumar, R. P.; Qiu, X. G. Optical Spectroscopy of the Weyl Semimetal TaAs. *Phys. Rev. B: Condens. Matter Mater. Phys.* **2016**, *93*, 121110.
(25) Soluyanov, A. A.; Gresch, D.; Wang, Z.; Wu, Q.; Troyer, M.; Dai, X.; Bernevig, B. A. Type-II Weyl Semimetals. *Nature* **2015**, *527*, 495−498.
(26) Liu, J.; Wang, H.; Fang, C.; Fu, L.; Qian, X. Van Der Waals Stacking-Induced Topological Phase Transition in Layered Ternary Transition Metal Chalcogenides. *Nano Lett.* **2017**, *17*, 467−475.
(27) Sun, D.; Wu, Z. K.; Divin, C.; Li, X.; Berger, C.; de Heer, W. A.; First, P. N.; Norris, T. B. Ultrafast Relaxation of Excited Dirac

Fermions in Epitaxial Graphene Using Optical Differential Transmission Spectroscopy. *Phys. Rev. Lett.* **2008**, *101*, 157402.

(28) Sun, Z.; Chang, H. Graphene and Graphene-Like Two-Dimensional Materials in Photodetection: Mechanisms and Methodology. *ACS Nano* **2014**, *8*, 4133−4156.

(29) Ma, Q.; Xu, S. Y.; Chan, C. K.; Zhang, C. L.; Chang, G. Q.; Lin, Y. X.; Xie, W. W.; Palacios, T.; Lin, H.; Jia, S.; Lee, P. A.; Jarillo-Herrero, P.; Gedik, N. Direct Optical Detection of Weyl Fermion Chirality in a Topological Semimetal. *Nat. Phys.* **2017**, *13*, 842−847.

(30) Osterhoudt, G. B.; Diebel, L. K.; Yang, X.; Stanco, J.; Huang, X.; Shen, B.; Ni, N.; Moll, P.; Ran, Y.; Burch, K. S. Colossal Photovoltaic Effect Driven by the Singular Berry Curvature in a Weyl Semimetal. **2017**, *https://arxiv.org/abs/1712.04951*. arXiv.org e-Print archive. https://arxiv.org/abs/1712.04951 (accessed Dec 13, 2017).

(31) Shekhar, C.; Nayak, A. K.; Sun, Y.; Schmidt, M.; Nicklas, M.; Leermakers, I.; Zeitler, U.; Skourski, Y.; Wosnitza, J.; Liu, Z. K.; Chen, Y. L.; Schnelle, W.; Borrmann, H.; Grin, Y.; Felser, C.; Yan, B. H. Extremely Large Magnetoresistance and Ultrahigh Mobility in the Topological Weyl Semimetal Candidate NbP. *Nat. Phys.* **2015**, *11*, 645−649.

(32) Wang, Q.; Li, C. Z.; Ge, S.; Li, J. G.; Lu, W.; Lai, J.; Liu, X.; Ma, J.; Yu, D. P.; Liao, Z. M.; Sun, D. Ultrafast Broadband Photodetectors Based on Three-Dimensional Dirac Semimetal Cd$_3$As$_2$. *Nano Lett.* **2017**, *17*, 834−841.

(33) Chan, C. K.; Lindner, N. H.; Refael, G.; Lee, P. A. Photocurrents in Weyl Semimetals. *Phys. Rev. B: Condens. Matter Mater. Phys.* **2017**, *95*, 041104.

(34) Belopolski, I.; Xu, S. Y.; Sanchez, D. S.; Chang, G.; Guo, C.; Neupane, M.; Zheng, H.; Lee, C. C.; Huang, S. M.; Bian, G.; Alidoust, N.; Chang, T. R.; Wang, B.; Zhang, X.; Bansil, A.; Jeng, H. T.; Lin, H.; Jia, S.; Hasan, M. Z. Criteria for Directly Detecting Topological Fermi Arcs in Weyl Semimetals. *Phys. Rev. Lett.* **2016**, *116*, 066802.

(35) Belopolski, I.; Yu, P.; Sanchez, D. S.; Ishida, Y.; Chang, T. R.; Zhang, S. S.; Xu, S. Y.; Zheng, H.; Chang, G.; Bian, G.; Jeng, H. T.; Kondo, T.; Lin, H.; Liu, Z.; Shin, S.; Hasan, M. Z. Signatures of a Time-Reversal Symmetric Weyl Semimetal with Only Four Weyl Points. *Nat. Commun.* **2017**, *8*, 942.

(36) Yu, R.; Weng, H. M.; Fang, Z.; Ding, H.; Dai, X. Determining the Chirality of Weyl Fermions from Circular Dichroism Spectra in Time-Dependent Angle-Resolved Photoemission. *Phys. Rev. B: Condens. Matter Mater. Phys.* **2016**, *93*, 205133.

(37) Koepernik, K.; Kasinathan, D.; Efremov, D. V.; Khim, S.; Borisenko, S.; Buchner, B.; van den Brink, J. TaIrTe$_4$: A Ternary Type-II Weyl Semimetal. *Phys. Rev. B: Condens. Matter Mater. Phys.* **2016**, *93*, 201101.

(38) Khim, S.; Koepernik, K.; Efremov, D. V.; Klotz, J.; Förster, T.; Wosnitza, J.; Sturza, M. I.; Wurmehl, S.; Hess, C.; van den Brink, J.; Büchner, B. Magnetotransport and de Haas−van Alphen Measurements in the Type-II Weyl Semimetal TaIrTe$_4$. *Phys. Rev. B: Condens. Matter Mater. Phys.* **2016**, *94*, 165145.

(39) Haubold, E.; Koepernik, K.; Efremov, D.; Khim, S.; Fedorov, A.; Kushnirenko, Y.; van den Brink, J.; Wurmehl, S.; Buchner, B.; Kim, T. K.; Hoesch, M.; Sumida, K.; Taguchi, K.; Yoshikawa, T.; Kimura, A.; Okuda, T.; Borisenko, S. V. Experimental Realization of Type-II Weyl State in Noncentrosymmetric TaIrTe$_4$. *Phys. Rev. B: Condens. Matter Mater. Phys.* **2017**, *95*, 241108.

(40) Yuan, H.; Liu, X.; Afshinmanesh, F.; Li, W.; Xu, G.; Sun, J.; Lian, B.; Curto, A. G.; Ye, G.; Hikita, Y.; Shen, Z.; Zhang, S.-C.; Chen, X.; Brongersma, M.; Hwang, H. Y.; Cui, Y. Polarization-Sensitive Broadband Photodetector Using a Black Phosphorus Vertical p−n Junction. *Nat. Nanotechnol.* **2015**, *10*, 707.

(41) Kim, J.; Lee, J. U.; Lee, J.; Park, H. J.; Lee, Z.; Lee, C.; Cheong, H. Anomalous Polarization Dependence of Raman Scattering and Crystallographic Orientation of Black Phosphorus. *Nanoscale* **2015**, *7*, 18708−18715.

(42) Song, J. C. W.; Levitov, L. S. Shockley-Ramo Theorem and Long-Range Photocurrent Response in Gapless Materials. *Phys. Rev. B: Condens. Matter Mater. Phys.* **2014**, *90*, 075415.

(43) Cai, X.; Sushkov, A. B.; Suess, R. J.; Jadidi, M. M.; Jenkins, G. S.; Nyakiti, L. O.; Myers-Ward, R. L.; Li, S.; Yan, J.; Gaskill, D. K.; Murphy, T. E.; Drew, H. D.; Fuhrer, M. S. Sensitive Room-Temperature Terahertz Detection *via* the Photothermoelectric Effect in Graphene. *Nat. Nanotechnol.* **2014**, *9*, 814−819.

(44) Mueller, T.; Xia, F. N. A.; Avouris, P. Graphene Photodetectors for High-Speed Optical Communications. *Nat. Photonics* **2010**, *4*, 297−301.

(45) Madejczyk, P.; Gawron, W.; Martyniuk, P.; Keblowski, A.; Pusz, W.; Pawluczyk, J.; Kopytko, M.; Rutkowski, J.; Rogalski, A.; Piotrowski, J. Engineering Steps for Optimizing High Temperature LWIR HgCdTe Photodiodes. *Infrared Phys. Technol.* **2017**, *81*, 276−281.

(46) Theocharous, E.; Ishii, J.; Fox, N. P. A Comparison of the Performance of a Photovoltaic HgCdTe Detector with That of Large Area Single Pixel QWIPs for Infrared Radiometric Applications. *Infrared Phys. Technol.* **2005**, *46*, 309−322.

(47) Engel, M.; Steiner, M.; Avouris, P. Black Phosphorus Photodetector for Multispectral, High-Resolution Imaging. *Nano Lett.* **2014**, *14*, 6414−6417.

(48) Youngblood, N.; Chen, C.; Koester, S. J.; Li, M. Waveguide-Integrated Black Phosphorus Photodetector with High Responsivity and Low Dark Current. *Nat. Photonics* **2015**, *9*, 247−252.

(49) Frenzel, A. J.; Homes, C. C.; Gibson, Q. D.; Shao, Y. M.; Post, K. W.; Charnukha, A.; Cava, R. J.; Basov, D. N. Anisotropic Electrodynamics of Type-II Weyl Semimetal Candidate WTe$_2$. *Phys. Rev. B: Condens. Matter Mater. Phys.* **2017**, *95*, 245140.

(50) Chen, D.; Zhao, L. X.; He, J. B.; Liang, H.; Zhang, S.; Li, C. H.; Shan, L.; Wang, S. C.; Ren, Z. A.; Ren, C.; Chen, G. F. Magnetotransport Properties of the Type-II Weyl Semimetal Candidate Ta$_3$S$_2$. *Phys. Rev. B: Condens. Matter Mater. Phys.* **2016**, *94*, 174411.

(51) Ezawa, M. Pseudospin-3/2 Fermions, Type-II Weyl Semimetals, and Critical Weyl Semimetals in Tricolor Cubic Lattices. *Phys. Rev. B: Condens. Matter Mater. Phys.* **2016**, *94*, 195205.

(52) Xu, X.; Song, Q.; Wang, H.; Li, P.; Zhang, K.; Wang, Y.; Yuan, K.; Yang, Z.; Ye, Y.; Dai, L. In-Plane Anisotropies of Polarized Raman Response and Electrical Conductivity in Layered Tin Selenide. *ACS Appl. Mater. Interfaces* **2017**, *9*, 12601−12607.

(53) Nanot, S.; Cummings, A. W.; Pint, C. L.; Ikeuchi, A.; Akiho, T.; Sueoka, K.; Hauge, R. H.; Leonard, F.; Kono, J. Broadband, Polarization-Sensitive Photodetector Based on Optically-Thick Films of Macroscopically Long, Dense, and Aligned Carbon Nanotubes. *Sci. Rep.* **2013**, *3*, 1335.

(54) Wang, J.; Gudiksen, M. S.; Duan, X.; Cui, Y.; Lieber, C. M. Highly Polarized Photoluminescence and Photodetection from Single Indium Phosphide Nanowires. *Science* **2001**, *293*, 1455−1457.

(55) Gassenq, A.; Gencarelli, F.; Van Campenhout, J.; Shimura, Y.; Loo, R.; Narcy, G.; Vincent, B.; Roelkens, G. GeSn/Ge Heterostructure Short-Wave Infrared Photodetectors on Silicon. *Opt. Express* **2012**, *20*, 27297−27303.

(56) Massicotte, M.; Schmidt, P.; Vialla, F.; Schadler, K. G.; Reserbat-Plantey, A.; Watanabe, K.; Taniguchi, T.; Tielrooij, K. J.; Koppens, F. H. Picosecond Photoresponse in Van Der Waals Heterostructures. *Nat. Nanotechnol.* **2016**, *11*, 42−46.

(57) An, X.; Liu, F.; Jung, Y. J.; Kar, S. Tunable Graphene-Silicon Heterojunctions for Ultrasensitive Photodetection. *Nano Lett.* **2013**, *13*, 909−916.